Talanta 277 (2024) 126376

Contents lists available at ScienceDirect

Talanta

journal homepage: www.elsevier.com/locate/talanta

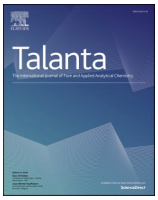

A novel aptasensor platform for the detection of carcinoembryonic antigen using quartz crystal microbalance

Aslı Erkal-Aytemur [a], İbrahim Ender Mülazımoğlu [b,**], Zafer Üstündağ [c], Mustafa Oguzhan Caglayan [d,*]

[a] Alanya Alaaddin Keykubat University, R.K. Faculty of Engineering, Fundamental Science, Antalya, Turkey
[b] Necmettin Erbakan University, A.K. Education Faculty, Chemistry Department, Konya, Turkey
[c] Kütahya Dumlupınar University, Faculty of Arts and Science, Department of Chemistry, Kütahya, Turkey
[d] Bilecik Seyh Edebali University, Faculty of Engineering, Department of Bioengineering, Bilecik, Turkey

ARTICLE INFO

Keywords:
Carcinoembryonic antigen
Electrochemical modification
Quartz crystal microbalance
Aptasensor

ABSTRACT

In this study, a quartz crystal microbalance (QCM) aptasensor for carcinoembryonic antigen (CEA), a well-known biomarker for various cancer types, was reported, utilizing two different aptamers. To achieve this, a nanofilm of 4-mercaptophenyl was electrochemically attached to gold-coated QCM crystal surfaces via the reduction of 4-mercaptobenzenediazonium salt (4 MB-DAT) using cyclic voltammetry. Subsequently, gold nanoparticles (AuNP) were affixed to this structure, and then aptamers (antiCEA1 and antiCEA2) modified with SH-functional ends bound to AuNPs completed the modification. The analytical performance of the CEA sensor was evaluated through simultaneous QCM measurements employing CEA solutions ranging from 0.1 ng/mL to 25 ng/mL. The detection limit (LOD) for CEA was determined to be 102 pg/mL for antiCEA1 and 108 pg/mL for antiCEA2 aptamers. Interday and intraday precision and accuracy tests yielded maximum results of 4.3 and + 3.8, respectively, for both aptasensors, as measured by relative standard deviation (RSD%) and relative error (RE%). The kinetic data of the aptasensors resulted in affinity values (K_D) of 0.43 ± 0.14 nM for antiCEA1 and 0.75 ± 0.42 nM for antiCEA2. These values were lower than the reported values of 3.9 nM and 37.8 nM for both aptamers, respectively. The selectivity of the aptasensor was evaluated by measuring the signal changes caused by alpha-fetoprotein (AFP), cancer antigen (CA-125), and vascular endothelial growth factor (VEGF-165) individually and together at a concentration of 500 ng/mL, resulting in a maximum 4.1 % change, which was comparable to precision and accuracy values reported in the literature. After confirming the selectivity of the aptamers, recovery experiments were conducted using spiked commercial serum samples to simulate real samples, and the lowest recovery value obtained was 95.4 %. It was determined that two different aptasensors could be successfully used for the QCM-based detection of CEA in this study.

1. Introduction

Tumor markers are detectable in bodily fluids and tissues and are used for cancer diagnosis and monitoring [1,2]. CEA is a tumor marker and a human cell surface glycoprotein [3] that becomes active in various tumors such as the colon [4], stomach [5], breast [6,7], pancreas [8], thyroid [9], and lung carcinomas [10], plays a role in cell adhesion and is expressed during human fetal development [11,12].

Elevated CEA values often correlate with an increase in cancer types. Monitoring CEA levels is a critical parameter during the treatment of these cancers, particularly in colon and stomach cancer. Decreases in CEA levels are also important during the cancer treatment, for deciding the termination of treatment or changes in treatment methods or dosage of the medicine. Post-surgical increases in CEA levels, also, indicate incomplete tissue clearance or metastasis [13].

A CEA level above 5 ng/mL in a healthy human body suggests potential risks of cancer or related diseases [14,15]. Therefore, the accurate, rapid, and precise determination of CEA concentration at very low levels of detection (LOD) is of utmost importance [16]. Most published medical applications for CEA detection predominantly employ

* Corresponding author.
** Corresponding author.
E-mail addresses: mulazimoglu@gmail.com (İ.E. Mülazımoğlu), mocaglayan@gmail.com (M.O. Caglayan).

https://doi.org/10.1016/j.talanta.2024.126376
Received 2 November 2023; Received in revised form 13 May 2024; Accepted 5 June 2024
Available online 9 June 2024

enzyme-linked immunosorbent assays (ELISAs) [17]. Additionally, studies on fluorescence [18], electrochemical [19], radioimmunoassay (RIA) [20], and immunoradiometric analysis (IRMA) [21] exist. Despite their strong selectivity, these immuno-tests require specific labels such as fluorescent molecules, radioactive elements, or enzymes to convert antigen-antibody binding into readable signals [22].

Furthermore, these techniques necessitate expensive equipment and skilled personnel, which may constrain their application [23,24]. Additionally, the use of radioactive elements as labels can lead to various detrimental effects on the human body, thus resulting in restricted work areas. Consequently, aptamer-based biosensor techniques, offering a rapid, highly sensitive, specific, and cost-effective approach, have been developed for CEA detection [25]. Aptamers are widely employed in various sensor domains owing to their flexibility, high repeatability, and ease of immobilization and regeneration [26–30]. Notably, electrochemical, surface plasmon resonance, and other methodologies are prominent among these [31,32]. In one of our previous studies, we advanced the plasmon method by developing an SPR-enhanced total internal reflection ellipsometry analysis [33]. On the other hand, the piezoelectric quartz crystal microbalance (QCM) technique is currently gaining well-deserved recognition in the literature due to its sensitivity, selectivity, accuracy, rapid response, and cost-effectiveness [34]. Therefore, we decided to develop and report for the first time a QCM aptasensor for CEA detection.

Numerous CEA analysis methods have been published in the literature. A recent comprehensive review has been published in 2020 [3]. Various studies have been highlighted including spectroscopic approaches [35], electrochemical methodologies [36–39], and photoelectrochemical (PEC) analysis [40,41] in this review. Extensive scrutiny has been conducted on articles published up until 2020. Furthermore, a subsequent analysis of post-2020 literature suggests ongoing endeavors to refine existing techniques, narrow the detection range, and decrease the limit of detection [42]. Notably, the literature also encompasses the utilization of surface plasmon resonance [32] and QCM [43] methods for CEA determination.

In this study, CEA analysis was conducted using QCM, a highly selective and sensitive technique. To construct an aptasensor platform, a thiol-bridged nanofilm was covalently bonded to the QCM crystal via the electrochemical reduction of diazonium salt, to create a more compact and smoother surface [44]. This surface modification, characterized by ellipsometry and cyclic voltammetry (CV) techniques, resulted in the formation of a film closely resembling a monolayer [45,46]. After the conjugation of gold nanoparticles (AuNPs) to this structure, CEA detection was accomplished by immobilizing two distinct aptamers onto it. The interaction between CEA aptamers and CEA was monitored in real-time to obtain analytical performance characteristics and conduct kinetic analysis. This study represents the first report on the development of QCM-based CEA aptasensors.

2. Experimental

2.1. Chemicals, reagents and equipment

In this study, the chemicals used were obtained from local representatives of Sigma Aldrich, Fluka, and Riedel-de Haen. Human serum (Cat No. H4522-20 ML) obtained from Sigma-Aldrich (USA), and used without dilution. Unless otherwise stated, all chemicals used were of at least analytical purity and were used as received without further processing. Ultra-pure water (UPW) used in the preparation of solutions was obtained from a Human Power +1 (Korea) device with a conductivity of 18.3 MΩ cm.

The aptamers used in the study were anti-CEA1 (5′- HS- $(CH_2)_6$ GGGGC GACGT TGAGA TTCCG CTTGT TGTTA TTAGT AGTCC CC- 3′) and anti-CEA2 (5′- HS- $(CH_2)_6$ ATACC AGCTT ATTCA ATTGG GGTAG GGGGC GAAGC GATAC CTTAA TCAGC-3′), with sequences as reported in the literature [47,48]. These aptamers were obtained from the Molbiol company in Germany.

QCM analyses were conducted using the SRS QCM 200 device (USA) with a 5 MHz AT-cut crystal with a diameter of 1 inch and electrode diameter of 0.55 inch with a sensitivity factor of 56.6 Hz cm^2/μg as stated by the manufacturer, and a crystal connection accessory that allowed for flow analysis. In sensor experiments, samples were delivered to the sensor surface at a flow rate of 20 μL/min using a peristaltic pump. Unless otherwise stated, measurements and analyses were performed at least in triplicate to ensure analytical conditions, and the relevant results were expressed as the arithmetic mean and standard deviation (±σ) of these replicates.

2.2. Preparation of nanofilms on QCM crystal using electrochemical method

Before functionalizing gold-coated QCM crystals with aptamers, their surfaces were modified using the electrochemical reduction method to obtain –SH terminated surfaces. To achieve this, the cyclic voltammetry (CV) technique was applied using the Ivium CompactStat (Netherlands) potentiostat/galvanostat device. Surface modification was carried out by covalently bonding 4-mercaptophenyl (4 MP) to the surface through the reduction of 4-mercaptobenzenediazonium salt (4 MB-DAT). The schematic representation of the modification is given in Fig. S1.

In summary, within an ice bath, 4-aminophenol (4ATP) was converted into 4 MB-DAT as follows [49]: 50 mg of 4ATP was weighed and dissolved in 10 mL of 0.5 M HCl. Then, 110 mg of $NaNO_2$ (69 g/mol), dissolved in 2 mL of pure water, was added to the ATP solution. The reaction was completed with the evolution of gas. The resulting diazonium solution (4 MB-DAT) was stored in the freezer for use in subsequent modifications.

Before modification, QCM crystals were cleaned by boiling in an NH_3/H_2O_2/Water (1:1:5, by volume) solution at 65 °C for 1 min and then dried [50]. Subsequently, the 4 MB-DAT solution was sent onto the crystals using a peristaltic pump for modification. In this process, the QCM crystal was connected as the working electrode to a three-electrode system, with $Ag/AgCl/KCl_{(sat)}$ as the reference electrode and platinum wire as the counter electrode. Additionally, Fig. S1 displays the cyclic voltammogram of 4 MB-DAT on the Au crystal electrode. In the first cycle, most of the diazonium salt on the electrode surface was reduced, completing a significant portion of the modification [51]. It was determined that the modification was fully completed in the second and third cycles [52]. The resulting nanofilm was named Au-4MP.

The AuNPs used in this study were synthesized using the citrate reduction method [53–55]. In summary, 150 mL of 2.2 mM trisodium citrate (Na_3cit) was heated to 90 °C and stirred at 500 rpm, while 1 mL of 25 mM $HAuCl_4$ was added drop by drop. The reaction was stopped by cooling when the colloidal solution turned reddish-brown. The colloidal solution, filtered through a 200 nm filter, was washed twice with ultrapure water (UPW) and twice with ethanol using a cooled ultracentrifuge (Hermle Z32HK, Germany). The pellet was then transferred to a 100 mL ethanol solution and stored in the cold for future use.

After functionalizing the QCM surface with –SH, AuNPs were spontaneously self-assembled onto the Au-4MP surface. To facilitate their dispersion, 10 mL of AuNPs were placed in an ultrasonic bath (Bandelin, Germany), and the Au-4MP surfaces were immersed in it for 4 h, leading to the modification [56]. The resulting surface was named Au-4MP-AuNP (Fig. S2).

Following the modification with AuNP, aptamers modified with SH at the 5′-terminus were immobilized onto each QCM crystal. To determine the optimal concentrations for immobilizing anti-CEA1 and anti-CEA2, 0.5, 1, 2, and 3 μM aptamers were interacted with the Au-4MP-AuNP surface for 2 h (in pH 7.4 PBS) [33]. Subsequently, QCM data were obtained using 25 ng/mL CEA to determine the optimal anti-CEA concentrations. Then, at the optimal concentration, anti-CEA1 and anti-CEA2 in PBS buffer solution were brought into contact with the

surface of Au-4MP-AuNP using a peristaltic pump for 2 h. This process resulted in the attachment of anti-CEA1 and anti-CEA2 to the Au-4MP-AuNP surface, leading to the formation of QCM crystals named Au-4MP-AuNP-antiCEA1 and Au-4MP-AuNP-antiCEA2, respectively. Subsequently, to block any remaining exposed surfaces, an ethanolic solution of 1 mM 6-mercaptohexanol was used [57].

2.3. Characterization of modified surfaces

The characterization of the obtained AuNPs was performed using Ultraviolet–Visible spectrophotometry (Shimadzu UV2550), scanning electron microscopy and Energy Dispersive X-ray Analysis (SEM and EDX, Nova, NanoSEM-650, Belgium), and transmission electron microscopy (TEM, JEOL Ltd., Tokyo, Japan).

For the characterization of the Au-MP nanofilm prepared through electrochemical diazonium salt reduction, ellipsometric thickness measurements (ELX-02C/01-R Ellipsometer, Germany) were used at each step. In this process, a 70° incident angle and monochromatic light at a wavelength of 532 nm were employed, and ellipsometric thickness was determined based on the Ψ and Δ values using a model of glass/Cr (3 nm)/Au (32 nm)/organic nanofilm/air [45,46,58,59]. The refractive indices for the respective layers were 2.2210 for the SF10 glass substrate, 3.0390 for the Cr layer, 0.4137 for the Au layer, 1.4600 for the nanofilm, and 1.0000 for air [50,58]. Additionally, X-ray photoelectron spectroscopy (XPS) characterization of the Au-MP-AuNP surface was conducted (XPS, PHI 5000-Versa Probe, Φ ULVAC-PHI.Inc., Japan/USA).

For electrochemical characterization, a BASI-MF-2014 (USA) gold electrode with a diameter of 1.6 mm was used instead of a QCM crystal. The modified surfaces were characterized using cyclic voltammetry (CV) with a 1 mM $K_3Fe(CN)_6$ redox probe.

2.4. CEA analysis

QCM analysis was conducted by sending CEA solutions at concentrations of 0.1, 0.5, 1, 5, 10, and 25 ng/mL (pH = 7.4; PBS) onto Au-4MP-AuNP-antiCEA1 and Au-4MP-AuNP-antiCEA2 QCM crystals using a peristaltic pump. The interaction between the aptamer and CEA was monitored online, and then, data was collected by passing only PBS buffer through the sensor chip under identical conditions to determine the dissociation reaction once equilibrium was reached. Instead of tracking the QCM frequency change (Δf), we recorded the mass change (Δm) over time. Following this, we input the sensitivity factor (C_f) for the 5 MHz cut-crystal and the device calculated and reported Δm using the Sauerbrey equation [60]. Since it was sufficient for the study's objectives to obtain a comparable response from the QCM device rather than the actual mass accumulated on the surface, no crystal calibration was performed to determine exact Δm. The obtained QCM response was then analyzed for complex formation kinetics using a single-site binding/complex formation kinetics model, and the aptamer's affinity (K_D) on the QCM surface was determined. Additionally, calibration curves were generated using the Δm values at equilibrium. To assess non-specific binding to the control aptamer, all procedures were applied similarly.

The accuracy and precision of the QCM sensor were determined for standard CEA analytes (0.5 and 10 ng/mL) under optimal conditions, both within the same day and across days (consecutive 5 days). Interference tests were conducted by sending CA125, VGF165, and AFP interferents individually and simultaneously onto the sensor.

For real sample analysis, commercial human serum samples were used as a simulated medium. CEA standards were spiked into the serum to achieve final concentrations of 1 and 10 ng/mL, and recovery values were determined.

3. Results and discussion

3.1. Characterization studies

Characterizations of the components used in the modification of the QCM surfaces in this study were conducted. SEM and TEM images of the AuNPs used for surface modification are presented in Fig. 1. The TEM image clearly shows nearly spherical AuNPs with sizes of approximately 10–20 nm (Fig. 1a). Additionally, a bulk SEM image of the produced AuNPs is provided in Fig. 1b, demonstrating a homogeneous distribution of the nanoparticles. Furthermore, using image processing software (Gwyddion Software) and segmentation algorithm [61,62], the size distribution of the particles was determined. It was found that approximately 80 % of the particles had sizes of 12 nm, while about 14 % had sizes of 20 nm. EDX spectrum of the gold nanoparticles is given in Fig. 1c. During the energy-dispersive X-ray analysis, it was observed that the typical absorption of metallic gold nanocrystals aligns with the literature, occurring at around 2.2 keV [63–65]. Fig. 1d displays the UV–Vis spectrum of colloidal (in water) AuNPs. These nanoparticles exhibited an absorbance peak at 525.4 nm, which was in good agreement with the calculated absorbance peak (approximately 525 nm) of 15 nm spherical nanoparticles in an aqueous colloid, according to Mie theory [66]. The characterization results confirmed the successful and uniform production of the AuNPs intended for modification.

In Fig. 2, high-resolution C_{1s} and S_{2p} narrow spectra of the Au slide and Au-4MP are provided. When fitting the C_{1s} region, three main peaks corresponding to aromatic C=C, and C–S were observed for Au-4MP at 285.6 eV and 283.5 eV, respectively [67]. The S_{2p} spectrum showed two main peaks for the thiol group on Au-4MP, with peaks at 164.5 eV ($S_{2p}^{1/2}$) and 163.4 eV ($S_{2p}^{3/2}$). These values were found to be following the literature, confirming the successful surface modification [68,69].

Furthermore, the characterization of the prepared surfaces was also performed using cyclic voltammetry [70–72]. In Fig. 3, cyclic voltammograms of 1 mM potassium ferricyanide (in 0.1 M KCl) on bare Au, Au-4MP, and Au-4MP-AuNP surfaces are shown. The anodic peak current values for the redox probe on Au, Au-4MP, and Au-4MP-AuNP were determined as 10.453 ± 0.093, 4.976 ± 0.016, and 6.793 ± 0.044 μA, respectively. As observed from the voltammogram, it confirms that the Au surface was modified first with 4-MP and then with AuNP.

The thickness of the Au-4MP nanofilm was confirmed through ellipsometric measurements, and the findings are presented in Table S1. To assess the uniformity and formation of the electrode surface layer, measurements were conducted at three distinct points, as outlined in the table. The average thickness of the nanofilm was determined to be 1.21 nm, with a standard deviation of 0.17 nm for the three points (n = 5). This result suggests the formation of a monolayer and an even distribution of the nanofilm during the first cycle of the CV. As the number of cycles increases in films produced by the diazonium reduction method, pinholes on the surface are initially filled, leading to the subsequent formation of multilayer films due to the impact of electrogenerated radicals [73,74]. Based on the observation that the thickness closest to monolayer formation occurs after the first cycle, it was determined that a single cycle is sufficient for sensor studies. This finding is in line with the results we previously reported elsewhere [33].

Aptamer concentration to be used for aptamer immobilization was optimized according to the QCM sensor response. When the response obtained with antiCEA1 and antiCEA2 aptamers was examined after interaction with 25 ng/mL CEA in Fig. S3, it was observed that the aptamer immobilized at a concentration of 1 μM provided sufficient response. Therefore, it was deemed appropriate to incubate 1 μM aptamer for 2 h during the immobilization of aptamers.

3.2. CEA analysis

Detection of CEA solutions in the range of 0.1 ng/mL to 25 ng/mL (in PBS, pH 7.4) was performed using the obtained QCM surfaces. Real-time

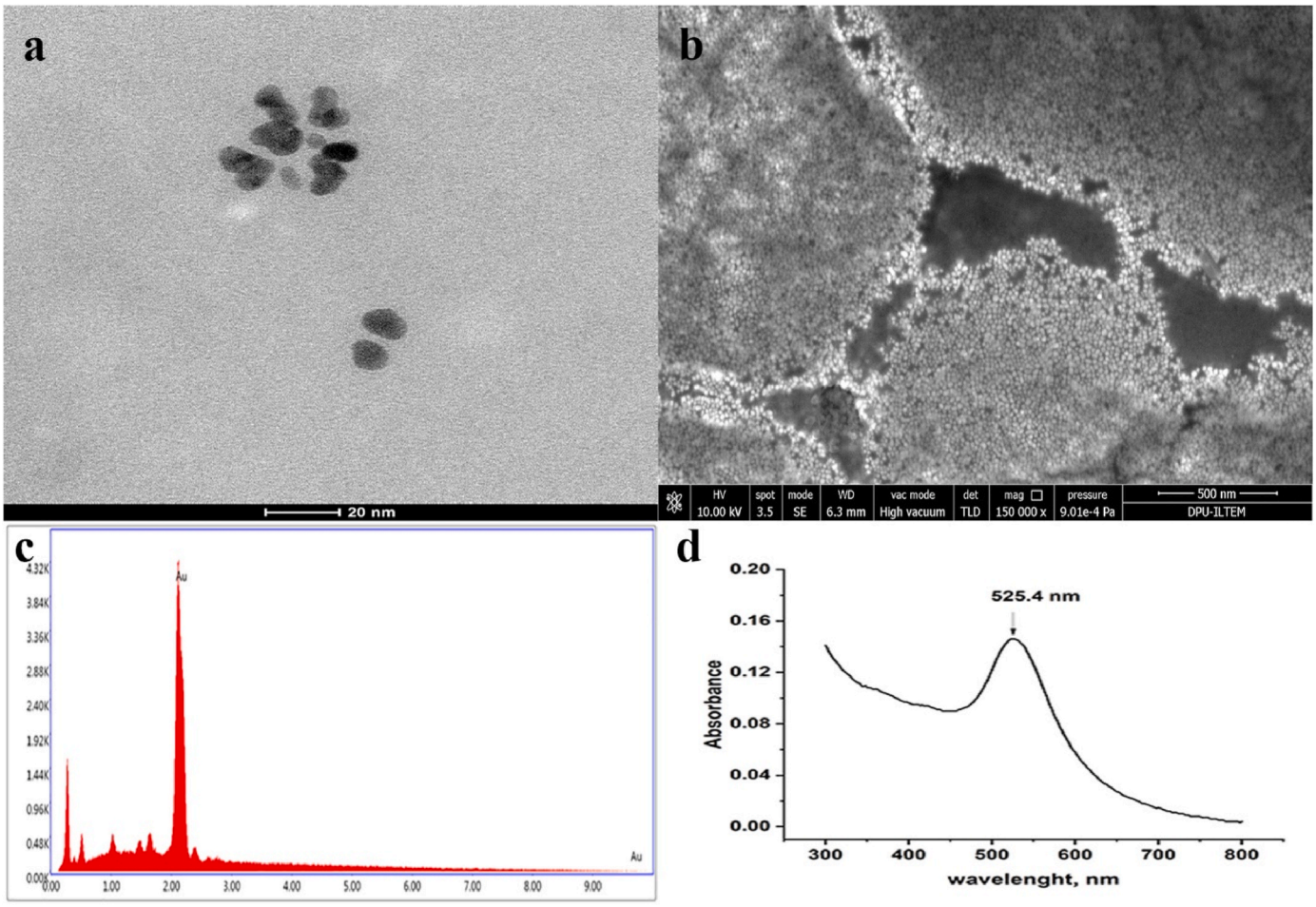

Fig. 1. TEM (a), SEM (b) image, EDX spectrum (c), and UV–Vis spectrum (d) of AuNPs.

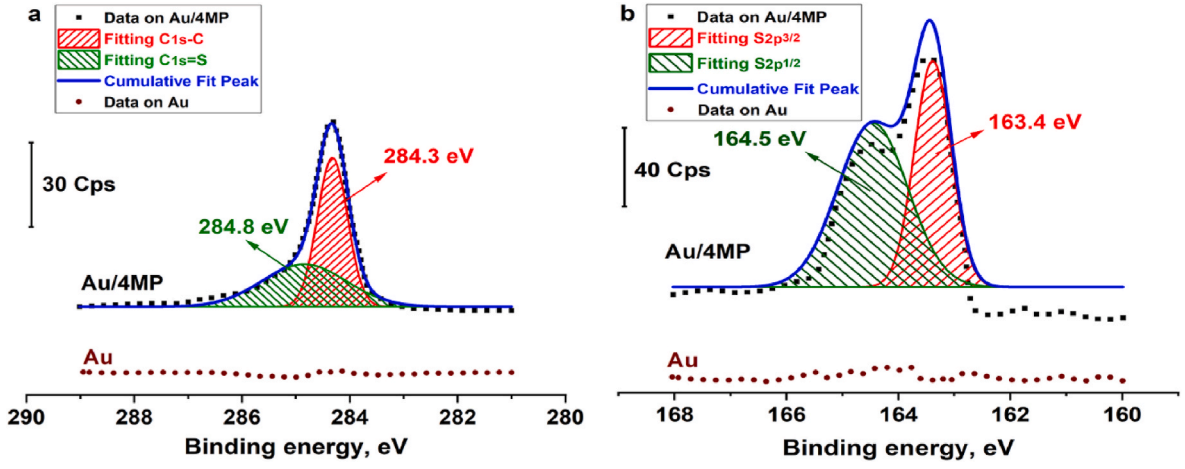

Fig. 2. High-resolution C_{1s} (a) and S_{2p} (b) narrow spectrum of the Au slide and Au-MP.

QCM sensograms (Δ-time) were obtained by interacting 0.1, 0.5, 1, 5, 10, and 25 ng/mL CEA solutions with the surfaces of two different aptamer-immobilized QCM sensors (Fig. 4). In both sensorgrams, it was observed that the binding between CEA aptamer and CEA reached equilibrium within the first 5 min after injection. Around the 40–50-min mark, a buffer solution (PBS, pH 7.4) was sent to the sensor surface alone to initiate the disassociation process. The analysis was concluded upon reaching equilibrium during the disassociation process.

As seen in Fig. 4, the Δm (μg/cm^2) values obtained on surfaces immobilized with antiCEA1 aptamer were somewhat higher (approximately 40 % higher for 25 ng/mL CEA) compared to the values obtained from surfaces immobilized with antiCEA2 aptamer. This difference was reflected in the detection limit of the antiCEA1 immobilized QCM sensor as well. The binding kinetics for both sensor platforms exhibited similar behavior at room temperature. The noise values obtained for 5 repetitions were approximately the same for both platforms and were found to

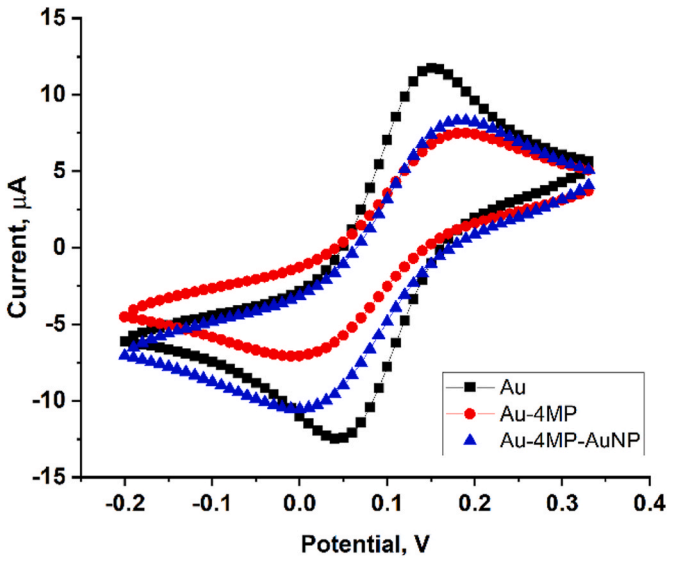

Fig. 3. CV voltammograms of 1 mM potassium ferricyanide in 0.1 mM KCl on bare Au, Au-4MP, and Au-4MP-AuNP electrode (scan rate is 200 mV/s, vs. Ag/AgCl(sat.)).

be small relative to the signal received. It is believed that the fluctuations that occurred during the waiting period after reaching equilibrium were due to small variations at room temperature.

Calibration curves for both QCM sensors were calculated using binding equilibrium values, and they are presented in Fig. 5. The interaction between aptamers and CEA resulted in a logarithmic calibration curve. The semi-logarithmic sensor calibration curves yielded determination coefficients (R^2) of approximately 0.99. To assess the number of binding sites, the obtained calibration curves were fitted to both Langmuir and Freundlich kinetics. Both fittings resulted in determination coefficients of 0.998 and above, suggesting that complex formation between CEA and the antiCEA aptamer adhered to both isotherms. Consequently, based on the results of the Langmuir isotherm, it is estimated that the CEA-antiCEA aptamer complex formation occurs via a single binding site.

The analytical parameters for the sensor are summarized in Table 1. The limit of detection (LOD) for antiCEA1, calculated from the calibration equation, $\Delta m = 0.25452 \times \log[CEA]+0.31227$, using the maximum standard deviation of $3\sigma = 0.06$ was 0.102 ng/mL. Similarly, for the other aptamer, LOD was calculated as 0.108 ng/mL using the equation $\Delta m = 0.15113 \times \log[CEA]+0.2659$ with $3\sigma = 0.12$. The quantification limits (LOQ, as 3xLOD) were calculated as 0.306 ng/mL for antiCEA1 and 0.324 ng/mL for antiCEA2 sensors. These sensor analytical performance values are in line with sensors used for CEA detection in the literature. A lower detection limit could have been expected for a QCM platform, but, due to the fluctuations in the sensorgrams possibly as a result of temperature-related variations, the LOD and LOQ values of the sensor turned out to be higher than expected. Nevertheless, despite these results, it can be concluded that the LOD and LOQ values are sufficient for practical application in CEA detection.

Using the advantage of real-time binding data obtained from QCM, the kinetics of complex formation and affinity were determined. For this purpose, the complex kinetics of both anti-CEA1 and anti-CEA2 aptamers were studied using QCM data, and the affinity constants were calculated (Fig. S4). The affinity constant (K_D) was reported solely from the binding curves, encompassing both the association/dissociation curves and using the k_{off} values determined from these curves. The goal here is to ascertain the K_D value as accurately as possible from the noisy QCM online data.

Fig. 6a and b shows the distribution of the determined K_D values for antiCEA1 and antiCEA2 aptamers, respectively. The K_D values calculated from association/dissociation data for antiCEA1 and antiCEA2 were 48 ng/mL (0.27 nM) and 90 ng/mL (0.5 nM), respectively, assuming a molecular weight of 180 kDa for CEA. As seen in Fig. 6a and b, the distribution of K_D values calculated from association/dissociation curves is wider compared to the K_D value obtained directly from association curves. This is because in QCM, over time and in long-term online measurements, the flow and environmental temperature can cause a drift in the measured values. This drift reduces the quality of model fitting and leads to a determination coefficient (in terms of R^2) below 0.90 during fitting. By directly substituting the relatively constant k_{off} values obtained only from association curves (0.2486 ± 0.0496 L/min and 0.2287 ± 0.0720 L/min, respectively) into the modeling, the distribution, considering the standard deviation, was found to be 78.05 ± 24.78 ng/mL (0.43 ± 0.14 nM) for antiCEA1 and 134.87 ± 74.7 ng/mL (0.75 ± 0.42 nM) for antiCEA2 aptamers. These values did not yield results comparable to the reported values of 3.9 nM and 37.8 nM for both aptamers. However, variations in the transducer type and measurement method can result in different affinity measurements when there is no mass transfer limitation on the surface [75].

In the next stage of the study, the precision and accuracy parameters of the proposed method and QCM sensors were examined. For this purpose, interday and intraday tests were conducted, and the results are summarized in Table 2. Intraday precision and accuracy results were obtained for 5 samples, reported as precision (relative standard deviation, RSD%) and accuracy (relative error, RE%). According to these results, for 0.5 and 10 ng/mL CEA, RSD% ranged from 1.9 to 4.3, while RE% ranged from −3.6 to 2.2. Interday analyses were conducted over

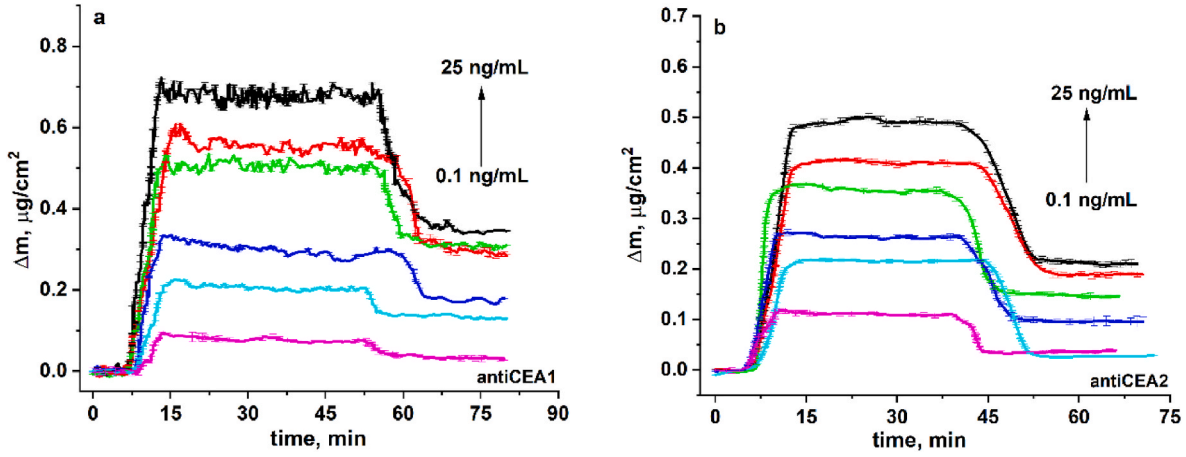

Fig. 4. Sensograms for the detection of CEA on QCM sensors immobilized with antiCEA1 (a) and antiCEA2 (b).

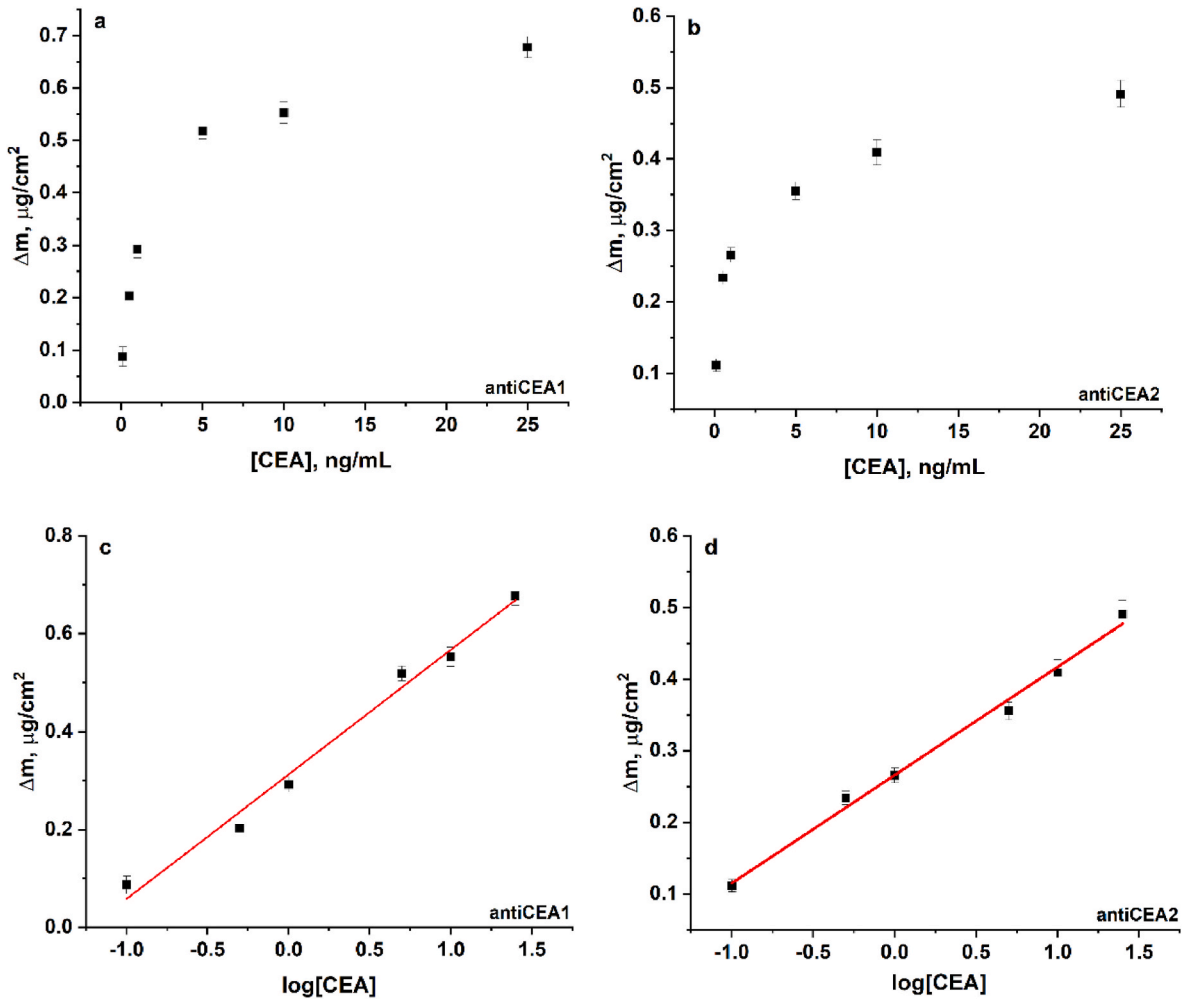

Fig. 5. Calibration curves for QCM sensors immobilized with antiCEA1 (a and c) and antiCEA2 (b and d), along with semi-logarithmic calibration plots.

Table 1
Data of the calibration curve for the developed methods (n = 5).

Analytical feature	Value	
	antiCEA1	antiCEA2
Regression equation	y = 0.25452x+0.31227	y = 0.15113x+0.2659
Standard error of the slope	0.01461	0.0067
Standard error of the intercept	0.0127	0.0060
Coefficient of determination	0.9870	0.9923
Linearity range (ng/mL)	0.1–25	0.1–25
Number of data points	6	6
Limit of detection (ng/mL) (S/N = 3)	0.102	0.108
Limit of quantification (ng/mL)	0.306	0.324

consecutive 5 days, and precision and accuracy results were obtained. According to these results, for 0.5 and 10 ng/mL CEA concentrations, RSD% ranged from 2.2 to 3.2, while RE% ranged from −1.4 to 3.8. No positive/negative RE bias was observed in both sensors. Precision and accuracy values for both aptasensors were below 5 %, indicating successful analytical results. The sensorgrams are given in Fig. S5.

Interference tests were conducted with the antiCEA1 aptamer, which demonstrated more successful sensor analytical performance criteria in terms of LOD and LOQ, against potential interferents such as AFP, CA125, and VEGF165. The percentage of Δm signal change obtained as a result of sending the interferents listed in Table 3 separately and together at a concentration of 500 ng/mL is provided. Interference experiments resulted in a positive bias in all measurements, but the values were below 5 % for both the interferent concentration and the CEA concentration. QCM sensograms of interference studies are given in Fig. S6a.

Finally, the analytical recovery performance of the developed sensor was evaluated by detecting CEA spiked into human serum at two different concentrations (Table 4). For this purpose, the QCM aptasensor platform immobilized with antiCEA1 and whose analytical performance was determined was used. In samples where 1 and 10 ng/mL CEA were spiked, the recovery percentages were a minimum of 95.4 %. This result is highly successful from an analytical perspective and demonstrates the ability to detect CEA from real samples using the QCM aptasensors developed in this study. The sensorgrams of the detection of spiked CEA in human serum samples using the QCM aptasensor are given in Fig. S6b.

4. Conclusion

This study presents the development of a QCM aptasensor for the detection of CEA using two different aptamers. The methodology involved electrochemically attaching a 4-mercaptophenyl nanofilm onto gold-coated QCM crystal surfaces through the reduction of 4 MB-DAT using cyclic voltammetry. Subsequently, gold nanoparticles (AuNPs) were employed to enhance the sensor's performance, and aptamers (antiCEA1 and antiCEA2) with SH-functionalized ends were employed to achieve specificity.

The analytical evaluation of the CEA sensor involved meticulous QCM measurements over a wide range of CEA concentrations, ranging

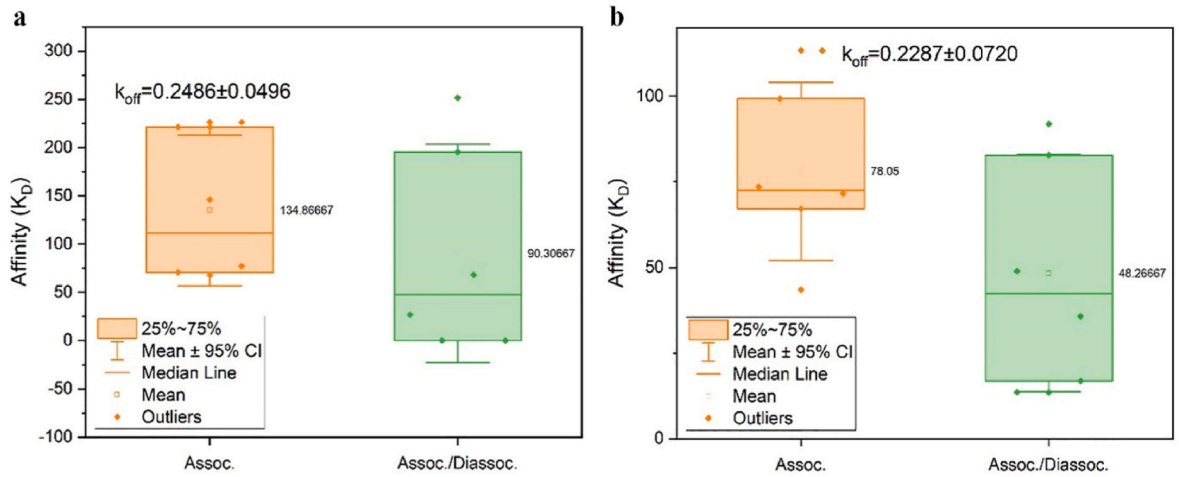

Fig. 6. Distribution of the determined K_D values for antiCEA1 (a) and antiCEA2 (b) aptamers.

Table 2
The precision and accuracy results of the proposed methods (mean ± σ).

[a]RSD% and RE %		Aptamer	[CEA], ng/mL	
			0.500	10.00
Intraday	**Resulting Value**	antiCEA1	0.486 ± 0.017	9.637 ± 0.184
		antiCEA2	0.511 ± 0.022	9.814 ± 0.224
	RSD%	antiCEA1	3.50	1.91
		antiCEA2	4.31	2.28
	RE%	antiCEA1	−2.80	−3.63
		antiCEA2	2.20	−1.86
Interdays[a]	**Resulting Value**	antiCEA1	0.494 ± 0.016	10.046 ± 0.227
		antiCEA2	0.519 ± 0.012	9.859 ± 0.218
	RSD%	antiCEA1	3.24	2.26
		antiCEA2	2.31	2.21
	RE%	antiCEA1	−1.20	0.46
		antiCEA2	3.80	−1.41

[a] RSD: Relative standard deviation; RE: Relative error, Interday studies for five consecutive days.

Table 3
The influences of some interferents at 500 ng/mL on the Δm% change of the signal acquired from 10 ng/mL CEA (for antiCEA1 platform).

Interferent	Signal change upon interferent addition (%)
AFP	+4.1
CA 125	+3.0
VEGF-165	+1.0
AFP + CA 125+ VEGF-165	+3.9

Table 4
Analytical recoveries of the CEA from human serum aliquots (N = 5) (for anti-CEA1 platform).

Spiked amount (ng/mL)	Detected amount of CEA (ng/mL)	Recovery (%)
1	0.954 ± 0.280	95.4
10	9.72 ± 0.32	97.2

from 0.1 ng/mL to 25 ng/mL. Notably, we determined detection limits (LOD) for CEA of 102 pg/mL for antiCEA1 and 108 pg/mL for antiCEA2 aptamers. These LOD values are comparable to and in line with the results reported in the literature for the detection of CEA (Table 5).

Furthermore, precision and accuracy assessments through interday and intraday testing revealed excellent results, with maximum relative standard deviation (RSD%) and relative error (RE%) values of 4.3 and + 3.8, respectively.

Table 5
- The determination range and limit of detection (LOD) values of CEA detection methods studied with various techniques in the literature.

Technique	Range, ng/mL	LOD, ng/mL	Reference
Photo-electrochemical immunoassay	0.02–50	0.00612	[76]
SERS[a]	1.0–1000	1.0	[77]
Fluorescence immunoassay	0.1–200	0.041	[78]
SPRe-TIRE[a]	0.01	500	[33]
Electrochemical immunoassay	1.0–40	0.0158	[79]
QCM immunoassay	1.0–15	0.86	[16]
QCM immunoassay	3.0–50	1.5	[80]
QCM immunoassay	0.1–100	0.09	[81]
QCM immunoassay	0.01–100	0.008	[43]
QCM aptasensor	0.1–25	0.102	this study

[a] SERS: Surface-enhanced Raman scattering, SPRe-TIRE: surface plasmon resonance-enhanced total internal reflection ellipsometry.

The kinetic analysis of the aptasensors yielded affinity values (K_D) of 0.43 ± 0.14 nM for antiCEA1 and 0.75 ± 0.42 nM for antiCEA2, underscoring their high binding affinities. Notably, these K_D values were notably lower than those previously reported for both aptamers.

The aptasensor's selectivity was validated through tests with other biomolecules, namely alpha-fetoprotein (AFP), cancer antigen (CA-125), and vascular endothelial growth factor (VEGF-165), both individually and in combination at a concentration of 500 ng/mL, resulting in a maximum signal change of only 4.1 %, in line with precision and accuracy values.

Furthermore, recovery experiments using spiked commercial serum samples demonstrated the aptasensors' practical applicability, with a minimum recovery value of 95.4 %. In summary, this study highlights the successful utilization of two distinct aptasensors for the sensitive and specific detection of CEA via QCM technology, offering promising prospects for advanced CEA detection methodologies.

CRediT authorship contribution statement

Aslı Erkal-Aytemur: Validation, Resources, Investigation. **İbrahim Ender Mülazımoğlu:** Writing – original draft, Validation, Supervision, Software, Project administration, Methodology, Data curation, Conceptualization. **Zafer Üstündağ:** Writing – review & editing, Writing – original draft, Validation, Supervision, Software, Resources, Project administration, Methodology, Data curation, Conceptualization. **Mustafa Oguzhan Caglayan:** Writing – review & editing, Writing – original draft, Validation, Supervision, Software, Resources, Project administration, Methodology, Investigation, Data curation,

Conceptualization.

Declaration of competing interest

The authors declare that they have no known competing financial interests or personal relationships that could have appeared to influence the work reported in this paper.

Data availability

Data will be made available on request.

Acknowledgment

This work was supported by TUBITAK (Scientific and Technological Research Council of Turkey) by project number 122Z678. Additionally, the authors would like to thank Kütahya Dumlupınar University and Necmettin Erbakan University for the financial contribution to this study through the BAP project numbered 2022–60 and 221410001, respectively.

Appendix A. Supplementary data

Supplementary data to this article can be found online at https://doi.org/10.1016/j.talanta.2024.126376.

References

[1] M.A. Virji, D.W. Mercer, R.B. Herberman, Tumor markers in cancer diagnosis and prognosis, CA A Cancer J. Clin. 38 (2) (1988) 104–126.
[2] Z. Tang, L. Li, L. Shen, X. Shen, S. Ju, H. Cong, Diagnostic value of serum concentration and integrity of circulating cell-free DNA in breast cancer, A Comparative Study With CEA and CA15-3, Laboratory Medicine 49 (4) (2018) 323–328.
[3] W. Xiang, Q. Lv, H. Shi, B. Xie, L. Gao, Aptamer-based biosensor for detecting carcinoembryonic antigen, Talanta 214 (2020) 120716.
[4] F.I. Téllez-Avila, S.M. García-Osogobio, [The carcinoembryonic antigen: apropos of an old friend], Revista de investigacion clinica; organo del Hospital de Enfermedades de la Nutricion 57 (6) (2005) 814–819.
[5] S.G. Derimanov, CEA in patients with stomach cancer, Eur. J. Cancer Clin. Oncol. 21 (11) (1985) 1378.
[6] K. Moar, A. Pant, V. Saini, M. Pandey, P.K. Maurya, Potential diagnostic and prognostic biomarkers for breast cancer: a compiled review, Pathol. Res. Pract. 251 (2023) 154893.
[7] L. Mariani, R. Miceli, S. Michilin, M. Gion, Serial determination of CEA and CA 15.3 in breast cancer follow-up: an assessment of their diagnostic accuracy for the detection of tumour recurrences, Biomarkers 14 (2) (2009) 130–136.
[8] X. Wang, P. Meng, S. Li, J. Tan, B. Su, Q. Cheng, X. Yang, Detection of two markers for pancreatic cancer (CEA, CA199) based on a nano-silicon sphere-cyclodextrin recognition platform, Alex. Eng. J. 75 (2023) 383–389.
[9] S. Turkdogan, V.-I. Forest, M.P. Hier, M. Tamilia, A. Florea, R.J. Payne, Carcinoembryonic antigen levels correlated with advanced disease in medullary thyroid cancer, Journal of Otolaryngology - Head & Neck Surgery 47 (1) (2018) 55.
[10] G. Wang, Z. Wang, X. Liu, Z. Tang, Y. Liu, X. Li, X. Zhou, H. Gong, Detection of CEA mRNA in patients with non-small cell lung cancer and it's significance, the Chinese-German, J. Clin. Oncol. 7 (11) (2008) 620–622.
[11] S. Oikawa, C. Inuzuka, M. Kuroki, Y. Matsuoka, G. Kosaki, H. Nakazato, Cell adhesion activity of non-specific cross-reacting antigen (NCA) and carcinoembryonic antigen (CEA) expressed on CHO cell surface: homophilic and heterophilic adhesion, Biochem. Biophys. Res. Commun. 164 (1) (1989) 39–45.
[12] W. Zimmermann, B. Weber, B. Ortlieb, F. Rudert, W. Schempp, H.-H. Fiebig, J. E. Shively, S. von Kleist, J.A. Thompson, Chromosomal localization of the carcinoembryonic antigen gene family and differential expression in various tumors, Cancer Res. 48 (9) (1988) 2550–2554.
[13] R. Takagawa, S. Fujii, M. Ohta, Y. Nagano, C. Kunisaki, S. Yamagishi, S. Osada, Y. Ichikawa, H. Shimada, Preoperative serum carcinoembryonic antigen level as a predictive factor of recurrence after curative resection of colorectal cancer, Ann. Surg Oncol. 15 (12) (2008) 3433–3439.
[14] B.A.A. Manaf, S.P. Hong, M. Rizwan, F. Arshad, C. Gwenin, M.U. Ahmed, Recent advancement in sensitive detection of carcinoembryonic antigen using nanomaterials based immunosensors, Surface. Interfac. 36 (2023) 102596.
[15] J. Han, Y. Li, J. Feng, M. Li, P. Wang, Z. Chen, Y. Dong, A novel sandwich-type immunosensor for detection of carcino-embryonic antigen using silver hybrid multiwalled carbon nanotubes/manganese dioxide, J. Electroanal. Chem. 786 (2017) 112–119.
[16] J. Liao, M. Lu, D. Tang, Enhanced sensitivity of quartz crystal microbalance immunosensor via back-conjugation of biofunctionalized magnetic beads with an external magnetic field, Biochem. Eng. J. 114 (2016) 276–282.
[17] L.K. Kiio, J.O. Onyatta, P.M. Ndangili, F. Oloo, C. Santamaria, L.M. Montuenga, D. N. Mbui, Ultrasensitive immunosensor for multiplex detection of cancer biomarkers carcinoembryonic antigen (CEA) and yamaguchi sarcoma viral oncogene homolog 1 (YES1) based on eco-friendly synthesized gold nanoparticles, Talanta 266 (2024) 124934.
[18] L. Guo, Y. Shi, X. Liu, Z. Han, Z. Zhao, Y. Chen, W. Xie, X. Li, Enhanced fluorescence detection of proteins using ZnO nanowires integrated inside microfluidic chips, Biosens. Bioelectron. 99 (2018) 368–374.
[19] X. Gu, Z. She, T. Ma, S. Tian, H.-B. Kraatz, Electrochemical detection of carcinoembryonic antigen, Biosens. Bioelectron. 102 (2018) 610–616.
[20] H. Kawamoto, H. Hara, J. Araya, A. Ichikawa, Y. Fujita, H. Utsumi, M. Hashimoto, H. Wakui, S. Minagawa, T. Numata, S. Arihiro, T. Matsuura, M. Fujiwara, S. Ito, K. Kuwano, Prostaglandin E-major urinary metabolite (PGE-MUM) as a tumor marker for lung adenocarcinoma, Cancers 11 (2019) 768.
[21] K.M. Sallam, A.S.A. El-Bayoumy, N.L. Mehany, Development of solid phase immunoradiometric assay for determination of carcinoembryonic antigen as a tumor marker, J. Radioanal. Nucl. Chem. 307 (2) (2016) 1375–1383.
[22] L. Xiao, A. Zhu, Q. Xu, Y. Chen, J. Xu, J. Weng, Colorimetric biosensor for detection of cancer biomarker by Au nanoparticle-decorated Bi2Se3 nanosheets, ACS Appl. Mater. Interfaces 9 (8) (2017) 6931–6940.
[23] R. Li, F. Feng, Z.-Z. Chen, Y.-F. Bai, F.-F. Guo, F.-Y. Wu, G. Zhou, Sensitive detection of carcinoembryonic antigen using surface plasmon resonance biosensor with gold nanoparticles signal amplification, Talanta 140 (2015) 143–149.
[24] T.-Y. Xing, J. Zhao, G.-J. Weng, J. Zhu, J.-J. Li, J.-W. Zhao, Specific detection of carcinoembryonic antigen based on fluorescence quenching of hollow porous gold nanoshells with roughened surface, ACS Appl. Mater. Interfaces 9 (42) (2017) 36632–36641.
[25] A. Futane, V. Narayanamurthy, P. Jadhav, A. Srinivasan, Aptamer-based rapid diagnosis for point-of-care application, Microfluid. Nanofluidics 27 (2) (2023) 15.
[26] M. Yüce, N. Ullah, H. Budak, Trends in aptamer selection methods and applications, Analyst 140 (16) (2015) 5379–5399.
[27] S. Catuogno, C.L. Esposito, V. De Franciscis, Aptamer-mediated targeted delivery of therapeutics: an update, Pharmaceuticals 9 (2016) 69.
[28] S.M. Nimjee, R.R. White, R.C. Becker, B.A. Sullenger, Aptamers as therapeutics, Annu. Rev. Pharmacol. Toxicol. 57 (1) (2017) 61–79.
[29] C. Perez-Gonzalez, D.A. Lafontaine, J.C. Penedo, Fluorescence-based strategies to investigate the structure and dynamics of aptamer-ligand complexes, Frontiers in chemistry 4 (2016) 33.
[30] N. Duan, S. Wu, S. Dai, T. Miao, J. Chen, Z. Wang, Simultaneous detection of pathogenic bacteria using an aptamer based biosensor and dual fluorescence resonance energy transfer from quantum dots to carbon nanoparticles, Microchim. Acta 182 (5) (2015) 917–923.
[31] J. Zheng, J. Wang, D. Song, J. Xu, M. Zhang, Electrochemical aptasensor of carcinoembryonic antigen based on concanavalin A-functionalized magnetic copper silicate carbon microtubes and gold-nanocluster-assisted signal amplification, ACS Appl. Nano Mater. 3 (4) (2020) 3449–3458.
[32] C. Guo, F. Su, Y. Song, B. Hu, M. Wang, L. He, D. Peng, Z. Zhang, Aptamer-templated silver nanoclusters embedded in zirconium metal–organic framework for bifunctional electrochemical and SPR aptasensors toward carcinoembryonic antigen, ACS Appl. Mater. Interfaces 9 (47) (2017) 41188–41199.
[33] A. Erkal-Aytemur, S. Şahin, Z. Üstündağ, İ.E. Mülazımoğlu, M.O. Caglayan, Determination of carcinoembryonic antigen (CEA) by surface plasmon resonance-enhanced total internal reflection ellipsometry (SPRe-TIRE), Instrum. Sci. Technol. 52 (2) (2024) 203–219.
[34] S. Akgönüllü, E. Özgür, A. Denizli, Recent advances in quartz crystal microbalance biosensors based on the molecular imprinting technique for disease-related biomarkers, Chemosensors 10 (2022) 106.
[35] Z. Qiu, J. Shu, D. Tang, Bioresponsive release system for visual fluorescence detection of carcinoembryonic antigen from mesoporous silica nanocontainers mediated optical color on quantum dot-enzyme-impregnated paper, Anal. Chem. 89 (9) (2017) 5152–5160.
[36] X. Zhou, S. Guo, J. Gao, J. Zhao, S. Xue, W. Xu, Glucose oxidase-initiated cascade catalysis for sensitive impedimetric aptasensor based on metal-organic frameworks functionalized with Pt nanoparticles and hemin/G-quadruplex as mimicking peroxidases, Biosens. Bioelectron. 98 (2017) 83–90.
[37] X. Zhou, S. Xue, P. Jing, W. Xu, A sensitive impedimetric platform biosensing protein: insoluble precipitates based on the biocatalysis of manganese(III) meso-tetrakis (4-N-methylpyridiniumyl)-porphyrinin in HCR-assisted dsDNA, Biosens. Bioelectron. 86 (2016) 656–663.
[38] H. Shu, W. Wen, H. Xiong, X. Zhang, S. Wang, Novel electrochemical aptamer biosensor based on gold nanoparticles signal amplification for the detection of carcinoembryonic antigen, Electrochem. Commun. 37 (2013) 15–19.
[39] P. Wang, Y. Wan, S. Deng, S. Yang, Y. Su, C. Fan, A. Aldalbahi, X. Zuo, Aptamer-initiated on-particle template-independent enzymatic polymerization (aptamer-OTEP) for electrochemical analysis of tumor biomarkers, Biosens. Bioelectron. 86 (2016) 536–541.
[40] L. Ge, W. Wang, T. Hou, F. Li, A versatile immobilization-free photoelectrochemical biosensor for ultrasensitive detection of cancer biomarker based on enzyme-free cascaded quadratic amplification strategy, Biosens. Bioelectron. 77 (2016) 220–226.
[41] W. Deng, L. Shen, X. Wang, C. Yang, J. Yu, M. Yan, X. Song, Using carbon nanotubes-gold nanocomposites to quench energy from pinnate titanium dioxide

nanorods array for signal-on photoelectrochemical aptasensing, Biosens. Bioelectron. 82 (2016) 132–139.
[42] X.-h. Wei, X. Qiao, J. Fan, Y.-q. Hao, Y.-t. Zhang, Y.-l. Zhou, M.-t. Xu, A label-free ECL aptasensor for sensitive detection of carcinoembryonic antigen based on CdS QDs@MOF and TEOA@Au as bi-coreactants of Ru(bpy)32+, Microchem. J. 173 (2022) 106910.
[43] L. Chi, C. Xu, S. Li, X. Wang, D. Tang, F. Xue, In situ amplified QCM immunoassay for carcinoembryonic antigen with colorectal cancer using horseradish peroxidase nanospheres and enzymatic biocatalytic precipitation, Analyst 145 (18) (2020) 6111–6118.
[44] R. Nigmatullin, D. Baleanu, E. Dinç, Z. Üstündağ, A. Solak, P. Kargin, Analysis of a nanofilm of the mercaptophenyl dıazonium modified gold electrode within new statistical parameters, J. Comput. Theor. Nanosci. 7 (2010) 562–570.
[45] Z. Üstündağ, A. Solak, EDTA modified glassy carbon electrode: preparation and characterization, Electrochim. Acta 54 (2009) 6426–6432.
[46] A. Turan, Z. Üstündağ, A. Solak, E. Kilic, A. Avseven, Characterization of a 2-Benzo [c]cinnoline modified glassy carbon electrode by Raman spectroscopy, electrochemical impedance spectroscopy, and ellipsometry, Electroanalysis 20 (2008) 1665–1670.
[47] M. Izabella Abreu de Melo, C. Rodrigues Correa, P. da Silva Cunha, A. Miranda de Góes, D. Assis Gomes, A. Silva Ribeiro de Andrade, DNA aptamers selection for carcinoembryonic antigen (CEA), Bioorg. Med. Chem. Lett 30 (15) (2020) 127278.
[48] Q.-L. Wang, H.-F. Cui, J.-F. Du, Q.-Y. Lv, X. Song, In silico post-SELEX screening and experimental characterizations for acquisition of high affinity DNA aptamers against carcinoembryonic antigen, RSC Adv. 9 (11) (2019) 6328–6334.
[49] K. Morita, A. Yamaguchi, N. Teramae, Electrochemical modification of benzo-15-crown-5 ether on a glassy carbon electrode for alkali metal cation recognition, J. Electroanal. Chem. 563 (2) (2004) 249–255.
[50] Z. Üstündağ, A. Turan, A. Solak, E. Kilic, A. Avseven, Analysis of 2-Benzo[c]cinnoline nanofilm at the gold surface, Instrum. Sci. Technol. 37 (2009) 284–302.
[51] S. Uluok, M. Erdoğan, I. Aşık, G. Kuzu, H. Ekşi, Z. Üstündağ, Nanocharacterization of the graphene oxide terminated platform on polycrystalline gold surface, J. Comput. Theor. Nanosci. 12 (2015) 1787–1794.
[52] A.A. İsbir-Turan, Z. Üstündağ, E. Kılıç, R. Güzel, Ö. Uçkan, A.O. Solak, Benzo[c] cinnoline and 2-benzo[c]cinnoline 6-oxide modified glassy carbon electrodes: electrocatalytic reduction of dioxygen in aqueous media, Instrum. Sci. Technol. 39 (2) (2011) 149–160.
[53] G. Frens, Controlled nucleation for the regulation of the particle size in monodisperse gold suspensions, Nat. Phys. Sci. (Lond.) 241 (105) (1973) 20–22.
[54] J. Turkevich, P.C. Stevenson, J. Hillier, A study of the nucleation and growth processes in the synthesis of colloidal gold, Discuss. Faraday Soc. 11 (0) (1951) 55–75.
[55] İ. Üstündağ, A. Erkal, T. Koralay, Y.K. Kadıoğlu, S. Jeon, Gold nanoparticle included graphene oxide modified electrode: picomole detection of metal ions in seawater by stripping voltammetry, J. Anal. Chem. 71 (7) (2016) 685–695.
[56] R. Güzel, Z. Üstündağ, H. Ekşi, S. Keskin, B. Taner, Z.G. Durgun, A.A.İ. Turan, A. O. Solak, Effect of Au and AuAg core–shell nanoparticles on the SERS of bridging organic molecules, J. Colloid Interface Sci. 351 (1) (2010) 35–42.
[57] H. Xia, F. Wang, Q. Huang, J. Huang, M. Chen, J. Wang, C. Yao, Q. Chen, G. Cai, W. Fu, Detection of Staphylococcus epidermidis by a quartz crystal microbalance nucleic acid biosensor array using Au nanoparticle signal amplification, Sensors (2008) 6453–6470.
[58] Z. Üstündağ, M.O. Çağlayan, R. Güzel, E. Pişkin, A.O. Solak, A novel surface plasmon resonance enhanced total internal reflection ellipsometric application: electrochemically grafted isophthalic acid nanofilm on gold surface, Analyst 136 (7) (2011) 1464–1471.
[59] A. Erkal, İ. Aşık, S. Yavuz, A. Kariper, Z. Üstündağ, Biosensor application of carbonaceous nanocoil material: preparation, characterization, and determination of dopamine and uric acid in the presence of ascorbic acid, J. Electrochem. Soc. 163 (5) (2016) H269.
[60] G. Sauerbrey, Verwendung von Schwingquarzen zur Wägung dünner Schichten und zur Mikrowägung, Z. Phys. 155 (1959) 206–222.
[61] Y. Zhan, G. Zhang, An improved OTSU algorithm using histogram accumulation moment for ore segmentation, Symmetry 11 (3) (2019) 431.
[62] N. Otsu, A threshold selection method from gray-level histograms, IEEE Transactions on Systems, Man, and Cybernetics 9 (1) (1979) 62–66.
[63] C. Wang, P. Singh, Y.J. Kim, R. Mathiyalagan, D. Myagmarjav, D. Wang, C.-G. Jin, D.C. Yang, Characterization and antimicrobial application of biosynthesized gold and silver nanoparticles by using Microbacterium resistens, Artificial Cells, Nanomedicine, and Biotechnology 44 (7) (2016) 1714–1721.
[64] İ. Üstündağ, S. Şahin, Determination of serotonin using gold nanorod-terminated carbonaceous electrode by differential pulse voltammetry, Chem. Pap. 77 (2023) 7447–7455.
[65] I.A. Kariper, M.O. Çağlayan, Z. Üstündağ, Heterogeneous Au/Ru hybrid nanoparticle decorated graphene oxide nanosheet catalyst for the catalytic reduction of nitroaromatics, Res. Chem. Intermed. 45 (2019) 801–813.
[66] S. Oldenburg, Light Scattering from Gold Nanoshells, 2000.
[67] A. de Morais, J. Alves, A. Lima, M. Lira-Cantu, A. Nogueira, Enhanced photovoltaic performance of inverted hybrid bulk-heterojunction solar cells using TiO 2/ reduced graphene oxide films as electron transport layers, J. Photon. Energy 5 (2015) 057408.
[68] N. Soltani, Q. Hassan, M. Noroozifar, K. Kerman, Au nanoparticles on 4-thiophenol-electrodeposited carbon surfaces for the simultaneous detection of 8-hydroxyguanine and guanine, Chemosensors 11 (2023) 326.
[69] E.Ç. Yeter, S. Şahin, M.O. Caglayan, Z. Üstündağ, An electrochemical label-free DNA impedimetric sensor with AuNP-modified glass fiber/carbonaceous electrode for the detection of HIV-1 DNA, Chem. Pap. 75 (1) (2021) 77–87.
[70] S.H. Mohammed Albayatı, Z. Üstündağ, P. Soylu, A novel molecularly imprinted electrochemical sensor for the ultrasensitive detection of tert-butylhydroquinone in edible oils, Anal. Biochem. 682 (2023) 115348.
[71] P. Deveci, B. Taner, Z. Üstündağ, Z. Kılıç, A. Solak, E. Özcan, Synthesis of some azacrown derivatives and fabrication of their nanofilms on the glassy carbon surface, J. Solid State Electrochem. 16 (2012) 985–992.
[72] I.E. Mülazımoğlu, Z. Üstündağ, E. Özkan, A.O. Solak, Covalent grafting of three flavonoids onto the glassy carbon electrode surface by cyclic voltammetry, Rev. Anal. Chem 30 (3–4) (2011) 177–185.
[73] P.A. Brooksby, A.J. Downard, Electrochemical and atomic force microscopy study of carbon surface modification via diazonium reduction in aqueous and acetonitrile solutions, Langmuir 20 (12) (2004) 5038–5045.
[74] A. Turan, E. Kilic, Z. Üstündağ, H. Ekşi, A. Solak, B. Zorer, Syntheses and modifications of bisdiazonium salts of 3,8-benzo[c]cinnoline and 3,8-benzo[c] cinnoline 5-oxide onto glassy carbon electrode, and the characterization of the modified surfaces, J. Solid State Electrochem. 16 (2012) 235–245.
[75] T. Johansson, Affinity measurements using quartz crystal microbalance (QCM), in: R. Kontermann, S. Dübel (Eds.), Antibody Engineering, Springer Berlin Heidelberg, Berlin, Heidelberg, 2010, pp. 683–693.
[76] R. Zeng, D. Tang, Magnetic bead-based photoelectrochemical immunoassay for sensitive detection of carcinoembryonic antigen using hollow cadmium sulfide, Talanta 219 (2020) 121215.
[77] M.C.C.G. Carneiro, A. Sousa-Castillo, M.A. Correa-Duarte, M.G.F. Sales, Dual biorecognition by combining molecularly-imprinted polymer and antibody in SERS detection. Application to carcinoembryonic antigen, Biosens. Bioelectron. 146 (2019) 111761.
[78] S. Lv, Y. Tang, K. Zhang, D. Tang, Wet NH3-triggered NH2-MIL-125(Ti) structural switch for visible fluorescence immunoassay impregnated on paper, Anal. Chem. 90 (24) (2018) 14121–14125.
[79] X. Zhao, W. Wang, L. Liu, Y. Hu, Z. Xu, L. Liu, N. Wu, N. Li, Microstructure evolution of sandwich graphite oxide/interlayer-embedded Au nanoparticles induced from γ-rays for carcinoembryonic antigen biosensor, Nanotechnology 30 (49) (2019) 495501.
[80] D.-Q. Tang, D.-J. Zhang, D.-Y. Tang, H. Ai, Amplification of the antigen–antibody interaction from quartz crystal microbalance immunosensors via back-filling immobilization of nanogold on biorecognition surface, J. Immunol. Methods 316 (1) (2006) 144–152.
[81] P.J. Jandas, J. Luo, A. Quan, C. Li, C. Fu, Y.Q. Fu, Graphene oxide-Au nano particle coated quartz crystal microbalance biosensor for the real time analysis of carcinoembryonic antigen, RSC Adv. 10 (7) (2020) 4118–4128.